

# Embedding a Water Vapor Radiometer Within a Deep Space Network Ka-band Receiver

Alan B. Tanner,<sup>\*</sup> James S. Border,<sup>\*</sup> Andre P. Jongeling,<sup>†</sup> Ezra M. Long,<sup>‡</sup> Erick Pereira,<sup>‡</sup> and Eli Lin<sup>‡</sup>

**ABSTRACT.** — An engineering model of a Ka-band monopulse receiver and cryostat cooler has been retrofitted with an Embedded Water Vapor Radiometer (EWVR) and then tested by observing the sky alongside an independent radiometer. Results demonstrate that atmospheric water vapor—which affects radio link performance by adding noise and path delay uncertainties—can be well measured from within a standard Deep Space Network (DSN) receiver without compromising telecommunication performance. Such a capability would offer a valuable tool to correct radio path delay uncertainties in spacecraft tracking data, as well as a continuous means of monitoring the atmospheric noise temperature contributions to communication link margins.

## I. Background

The Deep Space Network (DSN) presently maintains two Advanced Water Vapor Radiometers (AWVRs) located south of the Deep Space Station 25 (DSS-25) 34-meter beam waveguide (BWG) antenna at the Goldstone complex in California. This system was developed for the Cassini Gravity Wave Experiment, circa 2001, to measure the radio path delay induced by tropospheric water vapor during precision doppler tracking of the spacecraft. This same system is supporting Juno mission needs today—in an extended operations mode—where it continues to provide significant science benefit. Both Cassini and now Juno experience have shown that most of the line-of-sight radio path delay fluctuations caused by water, as measured by the Allan Standard Deviations at 10 to 10,000-second time scales, are typically measured and corrected with the AWVR data [1].

The AWVRs operate from pedestals separate than those of the main DSS-25 antenna. These are operated separately by radio science personnel. This poses operational cost in which each tracking observation must be separately prepared and coordinated with the DSS-25 antenna, and then later processed with analysis tools available presently only to the Planetary Radar and Radio Sciences Group on behalf of the Juno project. Few missions are

---

<sup>\*</sup> Tracking Systems and Applications Section.

<sup>†</sup> Communications, Tracking, and Radar Organization.

<sup>‡</sup> Communications Ground Systems.

The research described in this publication was carried out by the Jet Propulsion Laboratory, California Institute of Technology, under a contract with the National Aeronautics and Space Administration. © 2021 California Institute of Technology. U.S. Government sponsorship acknowledged.

able to support such efforts—even though many would benefit. Maintenance of the AWVR hardware and software has also posed ongoing costs to the DSN over the past 20 years, which has been difficult to manage due to the fact that the system was originally deployed for a specific experiment, without the documentation and planning that would normally accompany a DSN deliverable system.

The separate pedestals also pose performance costs. As illustrated in Figure 1, the AWVR is not entirely coincident with the DSS-25 antenna beam, and this causes a sampling error. This was a recognized compromise made while planning the Cassini project, as integration within the main BWG posed many more untested challenges that the Cassini project chose to avoid by deploying the independent, experimental system. Performance has been adequate, but this beam mismatch error remains a significant concern.

We envision that a preferable and more sustainable arrangement will be to embed the radiometer function into standard DSN receivers. By doing so, both the antenna mismatch problem and the costs of separate pedestals would be eliminated. With this simpler and more passive arrangement, the atmospheric noise and radio path delay would become widely available to the DSN and to DSN customers as a standard product. Such an Embedded Water Vapor Radiometer (EWVR) capability would offer a high-value diagnostic tool as well as a doppler tracking performance upgrade across the DSN.

In a prior study of the EWVR concept in 2000, the noise performance of a BWG antenna itself was examined by placing one of two AWVRs at the focal point of the DSS-13 antenna while making concurrent observations from the second AWVR located outside of the DSS-13 antenna [2]. Those tests revealed that although the 34-meter antenna added some anticipated radio noise via scattering from the subreflector support structure, such noise was minor and readily characterized as a smooth function of elevation and azimuth angles. These contributions are correctable in the water vapor measurement. The conclusion of that study was that the DSN antenna itself posed no obstacle to an EWVR function.

In a follow-on study to the DSS-13 experiment, however, stability tests of a standard DSN receiver demonstrated that the gain stability of a standard DSN Ka-band receiver was not sufficient for the radiometer function unless some reference load (e.g., Dicke switch) were

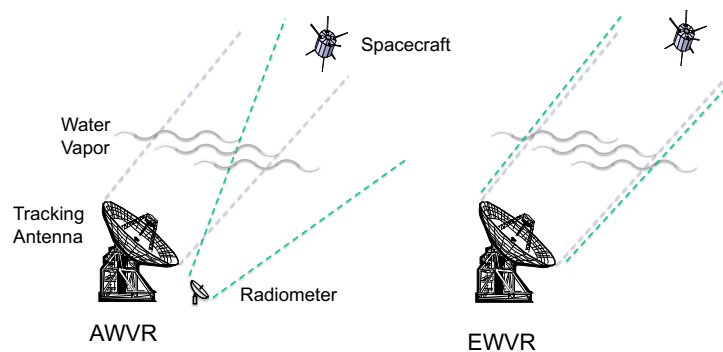


**Figure 1. The AWVR of the Cassini Gravity Wave Experiment is located south of the tracking antenna and therefore does not sample precisely the same atmosphere. A better arrangement would be to share the optical path with an Embedded WVR (EWVR).**

available [3]. At that time, this appeared to preclude the possibility that the WVR could share a receiver with the Ka-band telecom receiver. Compounding the problem was the fact that the WR-28 waveguide size of the DSN receiver does not pass the water vapor signal that is strongest at 22.2 GHz.

These two problems have since been resolved: (1) A solution to the “Dicke switch problem” emerged from separate work at Jet Propulsion Laboratory (JPL) concerning applications of the “pseudo-correlation radiometer” topology (so named by radio astronomers as an alternative to a correlator [4],[5]) in which the reference noise temperature is simultaneously amplified with the antenna signal using a hybrid arrangement of two low-noise amplifiers, as detailed below. And (2) the WR-28 waveguide limitation was remedied by a straightforward redesign of the septum polarizer that is used to separate left and right-hand circularly polarized (LCP and RCP) signals at the back of the monopulse assembly. As it happens, the size of the circular waveguide that is required for the monopulse function—in which the circular waveguide must be oversized in order to support the necessary asymmetric TE<sub>21</sub> waveguide modes at 34 GHz—is large enough to support the TE<sub>11</sub> mode at 22.2 GHz. This was fortuitous because it meant that the only necessary modification to the monopulse antenna feed was an extended passband polarizer replacement for the WR-28 polarizer. The design and fabrication of such a polarizer was completed in 2018 with JPL Research and Technology Development (R&TD) funding. WR-34 waveguide and amplifier componentry were also procured at that time. In this past year, and after some “trial and error” configurations of the radiometer topology, a reliable and practical design has now emerged. We report here on this design and test results and calibration, and conclude with a discussion of lessons learned and a path forward to implementation.

## **II. EWVR Design**

Figures 2–4 illustrate the layout and function of the EWVR within a DSN monopulse feed cryostat, as tested this year on the roof of building 238 at JPL. In Figure 2, the electrical function of the EWVR is explained as follows:

Reading from the left side of Figure 2, the antenna presents two outputs of RCP and LCP signals from the septum polarizing ortho-mode-transducer (OMT) located at the back of the antenna feed horn. In normal operation the RCP signal represents the main telecommunications signal from spacecraft. The LCP signal is much less frequently used. The water vapor signal from the atmosphere is unpolarized, so there is no preference, and for this reason the LCP port was selected for the EWVR function. The RCP port is unchanged in our design, and in either case, the goal of the present effort is to demonstrate that the EWVR can be implemented without degrading either RCP or LCP noise figure.

The key to sharing this path for telecom and EWVR functions is the manner in which the antenna signal is split using a magic-T hybrid, amplified in two paths of equal gain and length, and then recombined in a second magic-T. As configured in Figure 2, this topology presents the amplified antenna signal at the output of the second magic-T—in this case the summing arm of the magic-T—with the same noise figure and net gain of a single amplifier. This amplified antenna signal can then be passed along as the LCP telecommunications signal as before and without interruption by a Dicke switch. The

signal that enters the delta-arm of the first hybrid is otherwise negated and isolated from the summing arm of the second hybrid, and reappears instead at the delta arm of the second hybrid. This signal serves as the reference signal for the radiometer. By switching between the antenna and reference outputs of this hybrid arrangement, the Dicke switch function for the radiometer is effectively restored without significantly impacting the telecommunications link.

Minor imbalances that exist in the two amplifiers can affect the isolation between the reference and antenna signals, so care is required in the design to maintain this balance. Several different configurations were attempted in our EWVR developments before this final (and simplest) approach proved reliable and robust in this regard. Further details of these balancing issues are in the conclusion of this report (Section V).

In Figure 2, the reference signal for the EWVR originates in a matched WR-34 waveguide load that is located at an intermediate stage of the cryocooler vacuum housing. This stage is typically near 50 K in operation. This temperature level is thought to have some advantage in that 50 K is roughly in the midrange of anticipated antenna brightness temperatures to be measured. In Figure 2, two noise diodes can also be added to the reference signal to raise the reference noise temperature further. These reference signals offer a degree of redundancy useful for diagnostics of the EWVR. In practice, however, these temperatures need not be so warm, and in a future iteration, an 8-K reference is worth consideration, as will also be discussed in the conclusion, Section V.

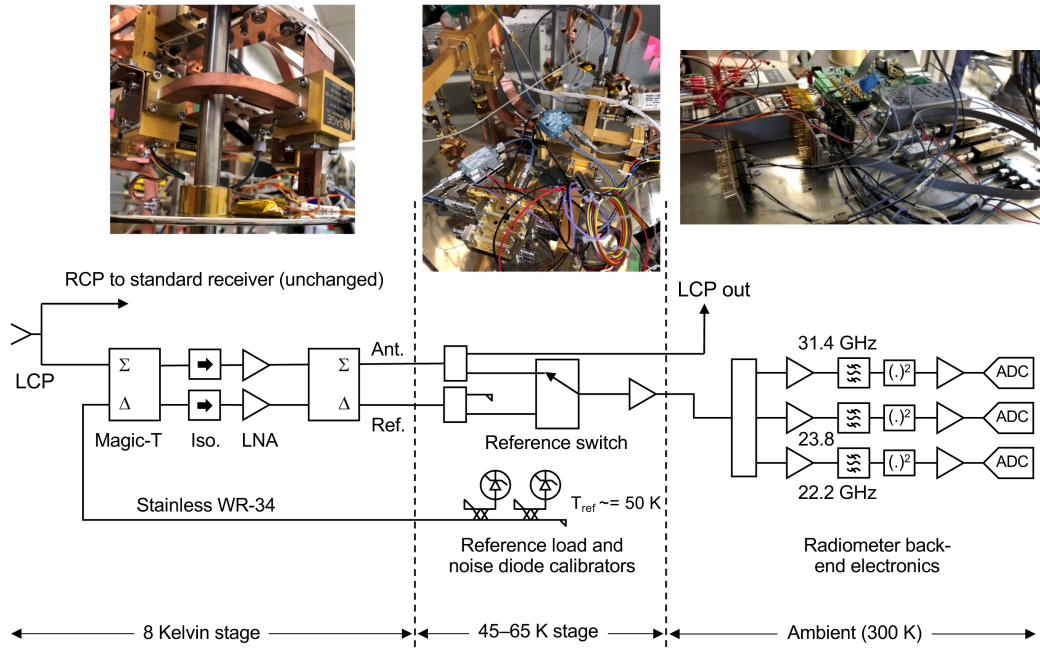


**Figure 2. EWVR block diagram. The LCP port of the antenna is split into two amplifier chains by a magic-T and then recombined in a second magic-T—all within the 8-K stage of the cryocooler housing—to produce amplified antenna and reference outputs. These recombined signals are then split again at the 50-K stage of the cooler, with the one LCP antenna signal passed out as the LCP telecom channel, and the other passed towards the radiometer, which switches between the LCP antenna and reference signals in a similar fashion to a Dicke switch.**



The remainder of the radiometer in Figure 2 consists of secondary amplifiers, bandpass filters, and detectors and digitizers to measure passbands at 22.2, 23.8, and 31.4 GHz. These are the same channels of the AWVR and in fact were implemented here using spare parts from the AWVRs. The data system of the EWVR presently consists of an Arduino controller that operates an Analog Devices 8-channel analog-to-digital converter (AD7779) evaluation circuit board located on the radiometer back-end assembly underneath and outside of the cryostat. A Python script is used within a Windows laptop computer to receive and record the data, which are transmitted by the Arduino to the PC via USB serial communications. Controls of the reference switch and noise diodes are asserted by the Arduino in a preprogrammed and repeating pattern.

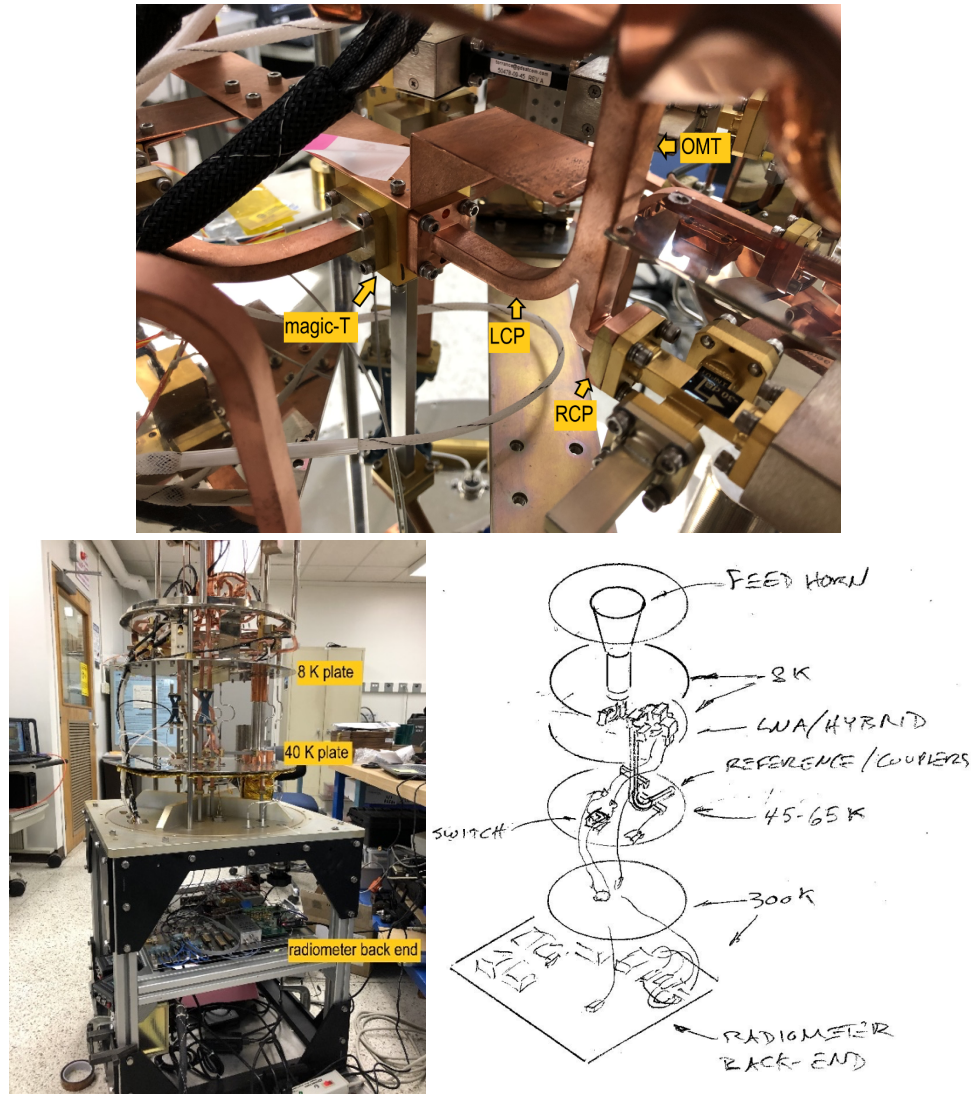


Figure 3. EWVR layout within cryostat.

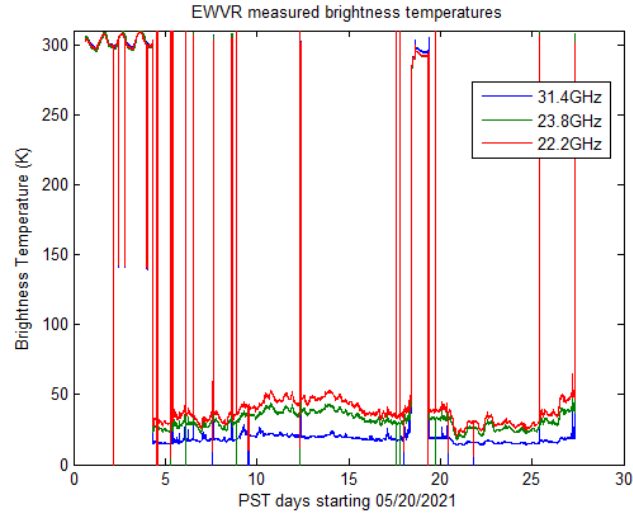


**Figure 4. EWVR on roof of JPL building 238, along with AWVR (lower left). The room containing the EWVR test has the skylight hatch that the DSN uses when testing its receivers (upper right photo).**

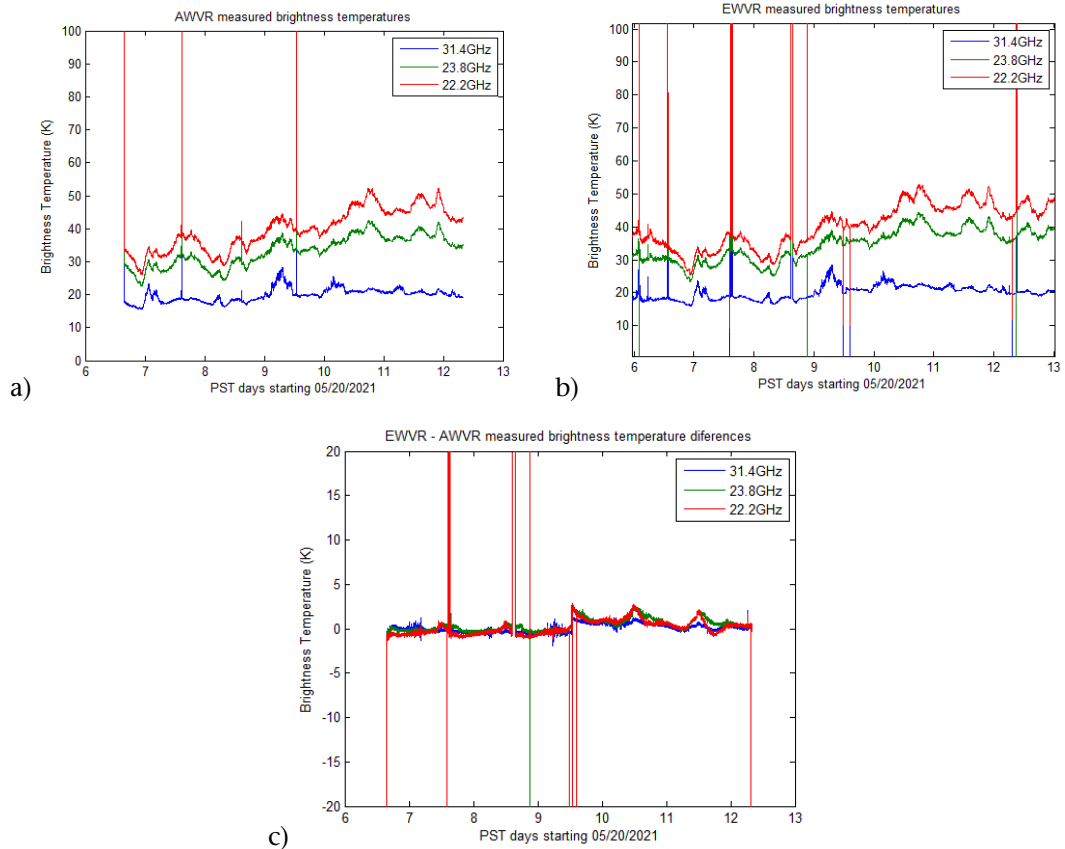
### III. Test Results

Figure 5 presents the brightness temperatures measured by the EWVR in the configuration of Figure 4 for nearly four weeks between May 20, 2021, and June 16, 2021. The observations of the sky began on May 23 following four days during which the ceiling window was shut. We see in these data the correct proportionality between 22.2 GHz, which is centered on the water vapor absorption spectral line; 23.8 GHz, on the hinge frequency just off the line center; and then 31.4 GHz, well away from the line center.

Between May 26, 2021, and June 1, 2021, one of the two AWVRs was made available following some maintenance activities at JPL, just prior to a return to Goldstone for Juno observations. Concurrent observations by the AWVR and EWVR are presented in Figure 6. The AWVR has a feed horn with a beamwidth that approximately matches that of the standard X/Ka horn of the DSN design, so only minor mismatches occur between the



**Figure 5. Antenna brightness measured by the EWVR between May 20, 2021 and June 16, 2021. The rooftop window was shut for the first four days and on day 18 (due to rain), and numerous ambient and liquid nitrogen target tests account for the remaining spikes that appear here.**



**Figure 6. (a) AWVR brightness temperature data collected between May 26, 2021, and June 1, 2021, prior to redeployment to Goldstone for Juno support, along with (b) corresponding time frame from Figure 5 of EWVR measurements. And (c) the difference between the EWVR and AWVR. (Note that the apparent shift on day 9.5 is due to a loss of cryostat temperature records after 9.5 days on the above timescale, which was patched using cryostat temperatures that were recorded 10 days later during similar weather conditions—see Figure 8.)**

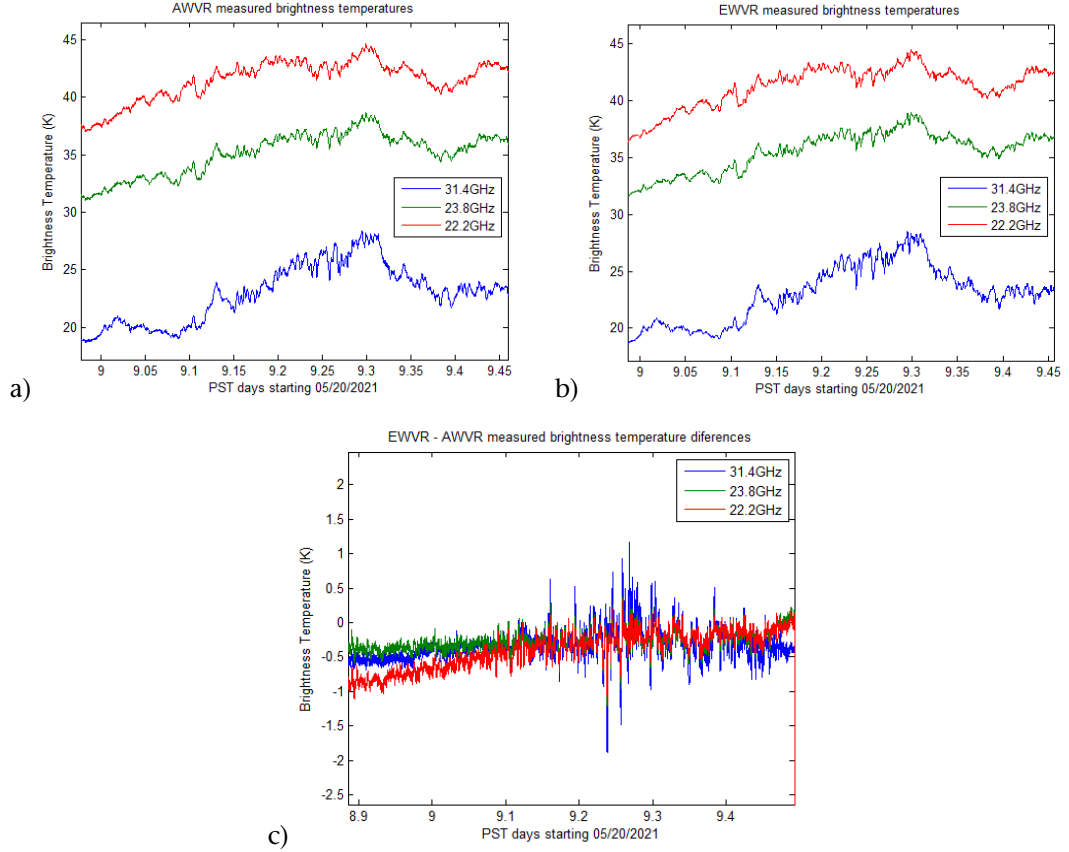


**Figure 7. Closeup segment from Figure 6 to show fine scale agreement during cloudy conditions (as evident when 31 GHz changes more than 22 GHz).**

EWVR and AWR. As can be seen, the match in Figure 6 is excellent. The difference between the two systems is generally less than  $\pm 1$  K, with a clear diurnal error component that is examined next in the calibration discussion. Figure 7 expands part of Figure 6 to further illustrate the excellent match between the AWR and EWVR. This segment was influenced by cloudy weather, which tends to raise the 31 GHz channel more than the 22.2 or 23.8 GHz channels.

#### IV. Calibration

An early calibration of the EWVR was based on the following formula:

$$T_B = \frac{C_{ant}}{C_{ref}} (T_{rec} + T_{ref}) - T_{rec} \quad (1)$$

where  $T_B$  is antenna brightness temperature;  $C_{ant}$  and  $C_{ref}$  are the digitized “counts” measured by the radiometer in the modes of the reference switch in Figure 2;  $T_{rec}$  is the receiver noise temperature; and  $T_{ref}$  is the reference noise temperature as measured with a temperature sensor on the  $\sim 50$  K matched load of Figure 2 and as plotted in Figure 8b. The form of (1) is the simplest and ideal case for the system of Figure 2. In practice, a variety of corrections to (1) should be anticipated as the system model is refined. For example, the

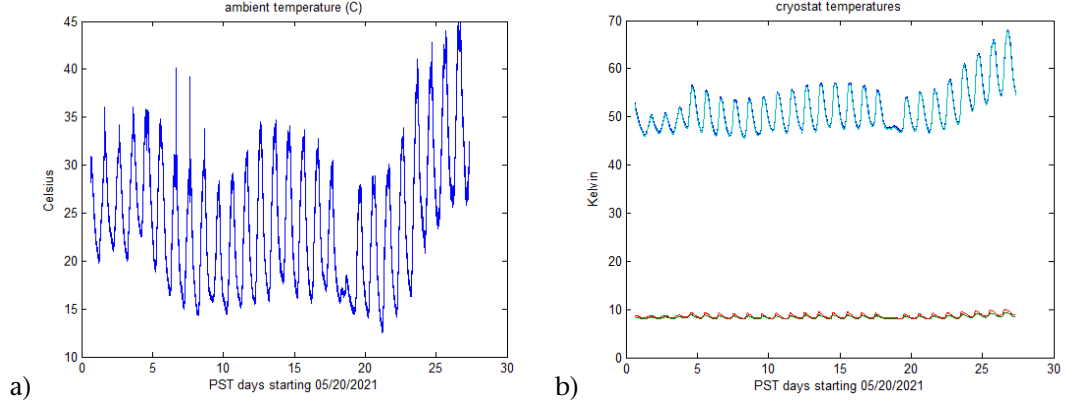


**Figure 8. Outside air temperature (a) and internal cryostat temperatures (b) for the 8-K stage and ~50-K intermediate stages of the cooler system. The timescale corresponds to that of Figure 5. (Note that the cryostat temperatures-logging software failed between 9.5 and 12.3 days, and data (b) here has been patched with a copy of the segment between day 19.5 and day 22.5, where a similar weather pattern prevailed. See corresponding note with Figure 6.)**

receiver noise term,  $T_{rec}$ , is known to change with the physical temperature of the receiver and can be expanded with formula to account for known effects if necessary. The reference temperature,  $T_{ref}$ , will also likely be biased by losses and thermal gradients within the system, which could be refined. And as with many radiometers, corrections for detector nonlinearities may be warranted. For the present data set, however, just two additional calibration terms were found to be necessary, and both are unique to the pseudo-correlation topology of Figure 2: (1) to account for leakage,  $L$ , of the antenna signal crossing into the reference signal, and vice versa; and (2) a switch balance ratio,  $R_{swbal}$ , to account for insertion loss imbalances between modes of the reference switch in Figure 2. These two terms modify (1) to arrive at the current working formula:

$$T_B = \frac{C_{ant}(1+L) - C_{ref}L/R_{swbal}}{C_{ref}(1+L)/R_{swbal} - C_{ant}L} (T_{rec} + T_{ref}) - T_{rec} \quad (2)$$

Table 1 summarizes the calibration coefficients that have been applied in (2) to produce the brightness temperatures of Figures 5–7. These parameters are reasonable given component specifications and were estimated as follows:

**Table 1. Calibration parameters for EWVR in (2), as applied in Figures 5, 6, and 7.**

	$T_{rec}$	$L$	$R_{swbal}$
22.2 GHz	19.5 K	0.0086	1.2
23.8 GHz	11.0 K	0.0056	1.08
31.4 GHz	18.5 K	0.0172	0.9

The leakage term,  $L$ , of Table 1 was directly measured using the noise diode signals available in the system. Figure 9a plots the raw “counts” measured in the 31.4 GHz channel, and Figures 9b and 9c examines the noise diode deflections to illustrate how this leakage term was calculated in Figure 9d from the ratio of noise diode deflections observed in the antenna mode divided by noise diode deflections observed in the reference mode.

Figures 9e and 9f further show, using a sky versus warm load contrast, that the leakage from the antenna into the reference equals the leakage from reference to antenna.

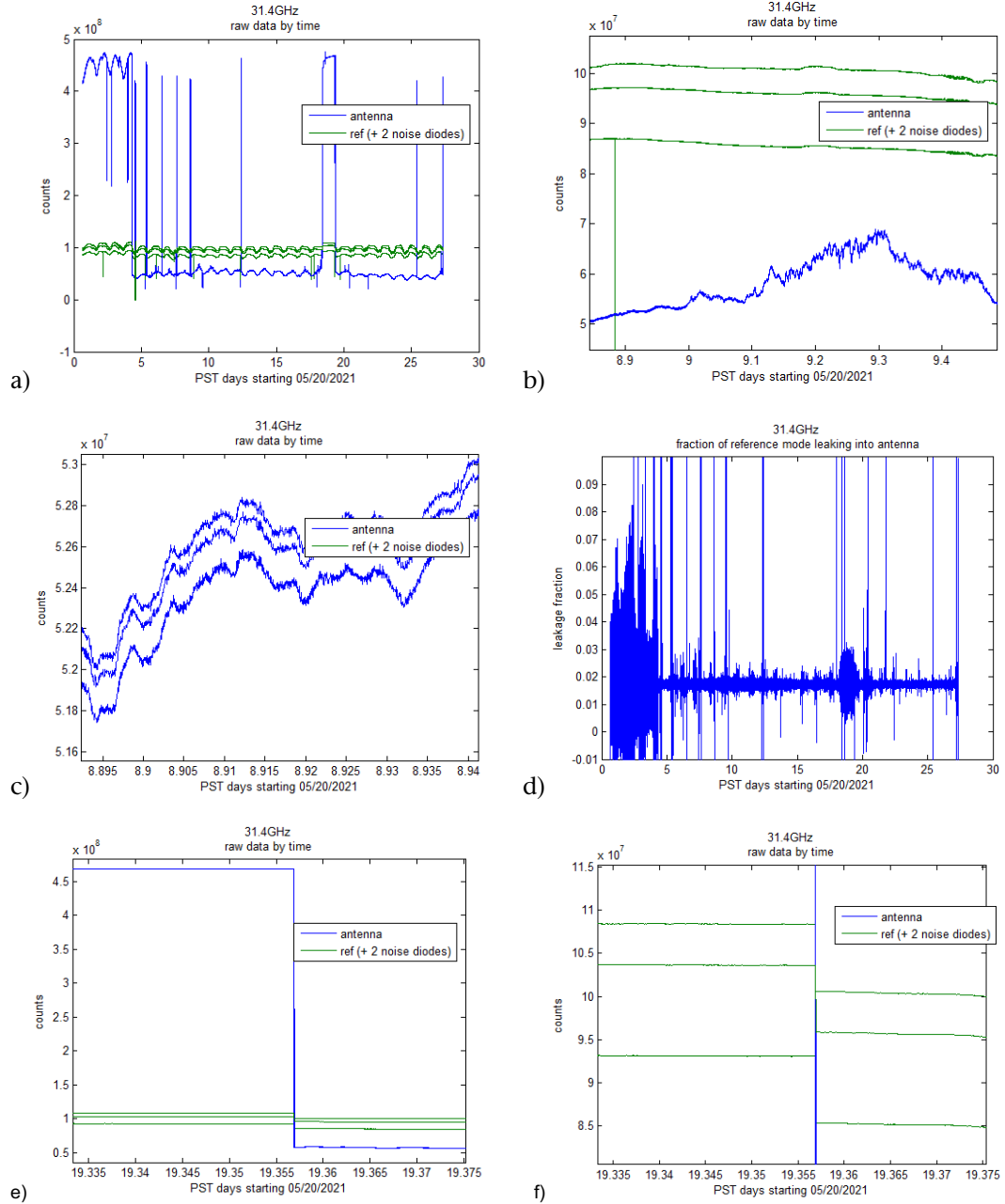


**Figure 9. A small amount of leakage from the reference port of the radiometer into the antenna port was measured by observing the noise diode deflections evident in the (a) raw counts; (b) expands the scale to show the three levels available with the reference, reference + noise diode 1, and then reference + noise diode 2 (three green traces); (c) expands further to show the corresponding leakage of these noise diodes also evident in the antenna counts (three blue traces); and (d) shows the calculated leakage estimated from the ratio of the antenna deflection over the reference deflection. This leakage is very stable near a level of 0.017, as applied in Table 1.**

In plots (e) and (f) we further confirm that the leakage from antenna to reference is also about 0.017, as measured from a sharp step as the antenna is uncovered ( $\sim 4e8$  counts drop in the antenna signal (e) versus  $\sim 7e7$  counts in the reference (f) to get  $7e7/4e8 = 0.017$ ).



Most important is that this leakage was found to be very constant over the span of the entire data set, as evident in Figure 9d. This is good because it indicates that the amplifier phase and amplitude balance are constant. This condition is key to the overall stability of the radiometer.

The switch balance,  $R_{swbal}$ , and receiver noise temperature,  $T_{rec}$ , terms of Table 1 were manually adjusted to attain agreement with a series of liquid nitrogen (LN2) and ambient target tests, which were conducted periodically throughout the timeline of Figure 5, and as expanded upon in Figure 10 and Figure 11. The need for the switch balance term became apparent during this process because it was not otherwise possible to simultaneously align the ambient  $\sim 300$  K and LN2  $\sim 80$  K data by adjusting only the receiver noise term in (1). The LN2 tests should produce roughly 80 K brightness, which is close enough in temperature to the internal matched load near 50 K that a large bias became obvious while attempting to calibrate the receiver noise alone in (1) from the ambient temperature target near 300 K. A second parameter was needed, and the switch balance stood out as a first-order problem: the switch that was used in these tests was from a conveniently available evaluation circuit that was known to be imperfectly balanced at the 0–1 dB level. The switch was also poorly matched and not specified for operation at 22.2 GHz, where indeed the greatest errors were noticed ( $1.2 = 0.8$  dB in Table 1). With this balance parameter in (2), it became possible to reproduce brightness temperatures that agreed reasonably well at both 80 and 300 K.

The LN2 data of Figure 10a are plotted with respect to the same timeline of Figure 5 for reference and are then expanded in Figure 10b by sample number wherever all three radiometer brightness temperatures are within the 70–90 K range. There were eight LN2 tests conducted in total, and one segment that was falsely detected as LN2 when rain water collected in the antenna on day 18. Figure 10b also adds the cryostat  $\sim 50$  K temperature and ambient room temperature in Celsius as relevant data for comparison. We see in

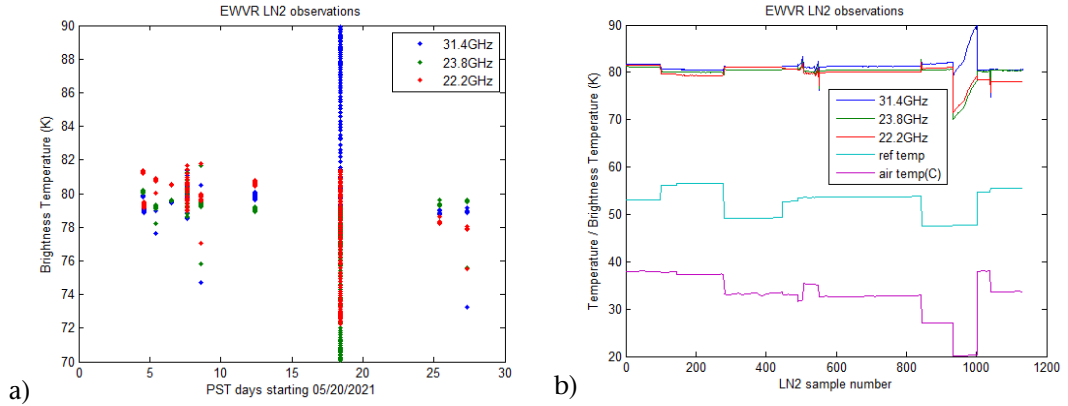


**Figure 10. (a) LN2 target tests were conducted occasionally throughout the May 23-to-June 16 timeline. (b) By plotting these same LN2 data by sample number (rather than time) the stability and repeatability of the LN2 data are evident. Included in (b) are the ambient air temperature in Celsius (purple trace in Celsius) and the intermediate cryostat temperature (magenta trace in kelvins), which is used as the radiometer reference temperature. The glitch near day 18 of (a) corresponds to samples 920–1050 of (b), and is an artifact caused by rain water that collected on the EWVR antenna’s Kapton window—which raised the antenna brightness to within the 70–90 K range used here to identify LN2 data.**

Figure 10b that the LN2 brightness temperatures agree within about  $\pm 1$  degree K along the 80 K level throughout these tests.

Figure 11a plots the ambient target data by sample number only. In this case there were fully four days at the start of the data set that dominate the horizontal scale of this plot—so Figure 11b further expands the scale around the shorter ambient target tests that accompanied the LN2 tests from Figure 10b. We see here that the ambient target data agree at the  $\pm 3$  K level. Actual temperatures of the warm targets (not plotted here) were logged, which also agree at the  $\pm 3$  K level.

The errors of both Figure 10 and Figure 11 don't yet appear to follow any consistent pattern relative to the ambient room or cryostat temperatures. This may be due to an incomplete characterization of the physical temperatures of the horn relative to the cryostat—which was not adequately recorded but were observed (felt) to vary greatly as sunlight heated the aluminum and copper components at the top of the cryostat. Temperatures there became hot to the touch, which is of order  $45^{\circ}\text{C}$  or more, versus nighttime cold points likely near  $10^{\circ}\text{C}$ . Such a range can affect standing waves between radome and OMT, if only via thermal expansion (rough calculation yields  $20^{\circ}$  electrical phase change across a  $35^{\circ}\text{C}$  change). Yet we can also note that the 3 K error observed at 300 K is greatly diminished to less than 1 K error near the  $\sim 20$  K antenna brightness in Figure 6 and Figure 7. Furthermore, such temperature swings are likely unique to the rooftop tests which place the receiver in direct sunlight. This would not be a problem within the pedestal room of a BWG antenna.

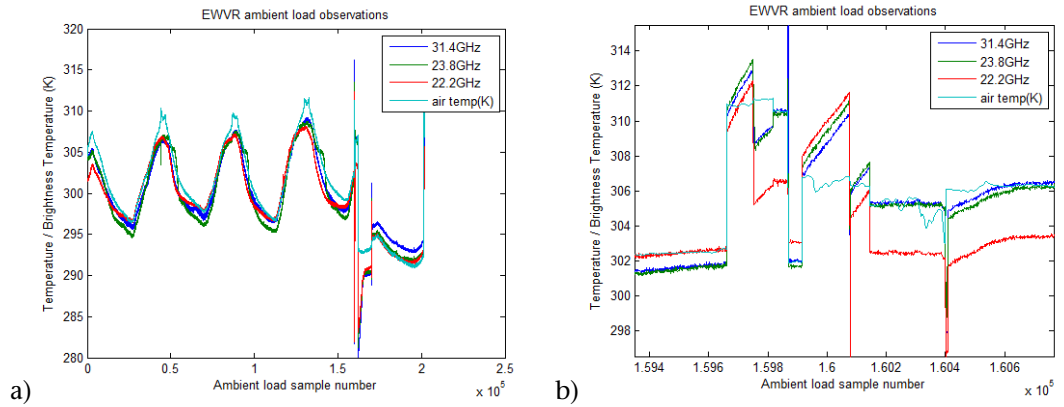


**Figure 11. Ambient target data as plotted by sample number, along with ambient air temperature measured by the radiometer data system underneath the cryostat. Plot (a) includes all data and is dominated by the first four days and day 18 of Figure 4. (b) expands the scale for eight separate warm load tests, which were conducted between days 4 and 7 at various time of day—and often in sunlight that tended to warm up the ambient target temperature during each test, as is evident. Overall, these data show a peak disparity of about 3 K in brightness temperature error when measuring warm targets under widely ranging conditions.**

## V. Conclusion and Path Forward

This work has demonstrated that the EWVR is not only feasible but also easy. The AWVR versus EWVR agreement of Figure 6 and Figure 7 is at a level of precision that rivals the precision of the AWVR without nearly the same precision of the thermal and electrical



controls that are contained within the AWVR. These results help to underscore the advantage of operating from an 8-K cryostat that is colder than the atmospheric noise temperature. This makes the atmospheric noise the dominant signal. The AWVRs by comparison operate near 310 K physical temperature and have receiver noise temperatures near 600 K. The atmosphere in that case is a very small fraction of 600 K, and for this reason the AWVRs demand much greater relative precision. In other words, a 1-K precision out of a ~20-K system noise temperature implies a 5% requirement (= easy), whereas 1 K out of 600 K implies 0.17% (= difficult).

There were some pitfalls uncovered in this project, as the design of Figure 2 did follow some less successful designs. Earlier work was based on the pseudo-correlation radiometer topologies that were closer in design to those described in literature [4],[5]. These employ phase switches placed in series with the RF paths between the hybrids so that the reference and antenna signals can be interchanged between output ports. This ultimately proved difficult to balance properly, due to imbalances in the phase switches and instability of coaxial cables. The original thought had been to bring both of the amplified RF signals out of the cryostat so that phase and amplitude could be fine-tuned outside of the cryostat with coaxial devices, and considerable effort was spent on the RF coaxial network within the radiometer back-end to accomplish this. In the end this proved unworkable due to the very long coaxial cables that carried the signals from the cryostat—which continuously crept in both amplitude and phase. That design was found to work for only a day or so before a new realignment of phase would be needed. The configuration of Figure 2 proved far more stable. Particularly impressive was the fact that the small leakage signature that was measured in the new configuration—of Figure 9d—was constant for the entire 27-day span. This is a very good indication that the configuration of Figure 2 is robust and reliable.

There was also no fine-tuning attempted with the configuration of Figure 2. The only effort made was to select two LNAs from the available parts with the closest gain patterns in the data sheets provided by the vendor. These data are compared in Figure 12 by overlaying the vendor data sheets of the amplifiers. Drain bias levels for the two LNAs—serial numbers SN019 and SN022—were regulated at identical levels of 1.2 V and 15 mA as well. Consistency of the component pieces and symmetry of the magic-T arrangement in Figure 2 certainly played a role in the excellent out-of-the-box performance, in terms of the low leakage factors in Table 1. As far as the EWVR function is concerned the current performance needs no further improvements.

In terms of the LCP telecommunication channel performance, there appears to be no showstoppers yet associated with the EWVR, although some improvements will be needed in some of the component selections. The impact on the LCP receiver noise figure is the main concern, and the only fundamental issue thus far is how well the two amplifiers of Figure 2 can be balanced between the magic-Ts in order to isolate signal leakage from the reference arm of the radiometer into the communications signal.

To measure the EWVR impact on LCP telecommunications noise performance, the LCP noise was independently tested by conventional means using a spectrum analyzer via the LCP out port of Figure 2. Upon completion of the EWVR tests, an identical follow-on test was then conducted after the hybrid magic-T of Figure 2 was removed, and the same two

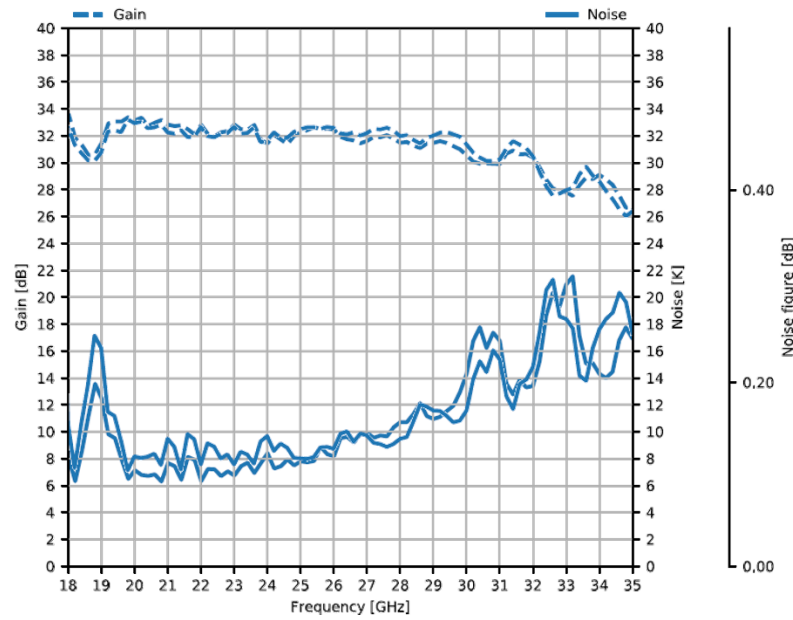


**Figure 12. Gain and noise figure data for the two LNAs of the EWVR, as provided by the vendor for 4 K operating temperature, are overlaid here to show that although the two amplifiers (serial numbers SN019 and SN022 of Low Noise Factory model LNF-LNC19\_34WA) are well matched, there is a spectral oscillation above 28 GHz where some mismatch can be anticipated.**

LNAs were attached directly to the LCP and RCP ports of the OMT. This test offers an objective assessment of the marginal change of noise figure with and without the EWVR. Results are presented in Figure 13.

In Figure 13 we see that most of the noise figure spectra (which, we should note, were subject to a passband limitation of an external amplifier that obscured the 22 GHz results) are unaffected by the EWVR, but there are spectral excesses near 31 GHz, 32 GHz, and 33 GHz. These excesses evidently coincide with spectral oscillations that exist in the amplifier gain of Figure 12. Where these spectra oscillate in Figure 12 the balance between the amplifiers is degraded—especially where the slope of gain versus frequency is large. This underscores the fact that amplifier balance will be necessary in order to share the EWVR with the telecommunications signal. This also makes it clear that amplifier performance should be optimized for the telecom band—as has always been the case for the DSN. The EWVR is otherwise far more tolerant of errors near 22 GHz.

The commercial amplifiers purchased for these tests are not the ideal choice for the DSN's needs, as they exhibit rather high noise figure (of order 19 K near 32 GHz) compared with state-of-the-art noise LNAs (near 10 K) otherwise available to the DSN. The EWVR function does not require exceptionally low receiver noise, so this will permit trades in which 32 GHz performance is optimized at the expense of performance near 22.2 GHz. LNA designs typically involve such trades, so this poses no new technology challenge. This also holds for the performance of ferrite isolators—for which bandwidth versus isolation performance is a well-known trade.

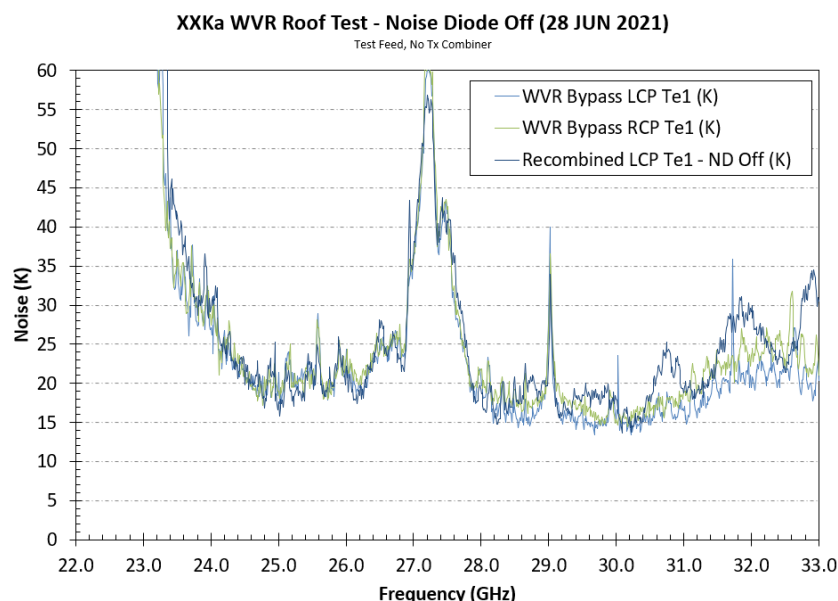


**Figure 13. Noise temperature measurements of the EWVR as configured in Figure 1 and using two amplifiers and the magic-Ts are compared here with measurements made of the individual amplifiers after placing the same two amplifiers at the RCP and LCP ports and bypassing the EWVR altogether. Note that the hybrid combination (recombined LCP) shows two peaks of ~5 K excesses of the noise near 31 GHz and 32 GHz, which coincide with steep spectral features evident in Figure 12.**

Another design choice that could reduce the impact of the reference load leakage into the LCP signal would be to reduce the temperature of the reference load to 8 K rather than 50 K, so that a small leakage would be at a correspondingly lower level. The reference load would be relocated to the 8 K stage of the cryocooler to make this change—which would actually simplify the overall system by eliminating the stainless waveguide section of Figure 2. A test of such a configuration would be warranted though, as the colder reference will also need to be characterized with proportionately better precision.

Other details of the EWVR design that deserve attention in an operational system concerns mismatches of the switch in Figure 2, which was a reflective pin diode switch with high reflections from inactive ports. This switch produced noticeable shifts in the LCP port signal as standing waves induced by the switch propagated back towards the LNA outputs. This can be corrected by either padding or isolating the switch inputs to reduce these reflections. Amplitude imbalances of the switch itself would easily be reduced by better part selection (the switch employed here was from an evaluation product not meant for operational use).

Another comment worth adding here is that the LCP receiver path does not presently include any passband filter. Existing telecommunications configurations of the standard DSN receivers generally include such filters. The original reason to include such filters in the front-end amplifier will need to be revisited, as there is at present little apparent need for them within the first LNA stage. Radio interference would pose one possible argument for such filters (to block intermodulation within an LNA from a very strong out-of-band source). Yet there is at present no indication that this is a real threat: The AWVRs, for

example, have very broadband gain in the LNA, and in 20 years there has never been any evidence of radio interference in these systems.

Lastly there is another, and as yet untested, hybrid configuration that would use two 3-dB couplers instead of the two magic-Ts of Figure 2. The advantage of this approach is superior impedance matching to the amplifier elements. Three-dB couplers are also known as 90-degree hybrid splitters, and from any one port, the round-trip reflection from a coupled port will be  $180^\circ$  out of phase with the uncoupled port. When two amplifiers present identical mismatches, the two reflections tend to cancel one another, which results in an improved match. Figure 14 shows coupler components that were tested for this possibility and found to be electrically well suited to the task but mechanically somewhat more difficult to integrate due to the length of the couplers. Future test of this possibility may be warranted. For the time being, however, the design of Figure 2 includes isolators to ensure a reliable amplifier match. Magic-Ts have an inherent advantage of being physically symmetric as well, so this design option is not yet clear-cut.

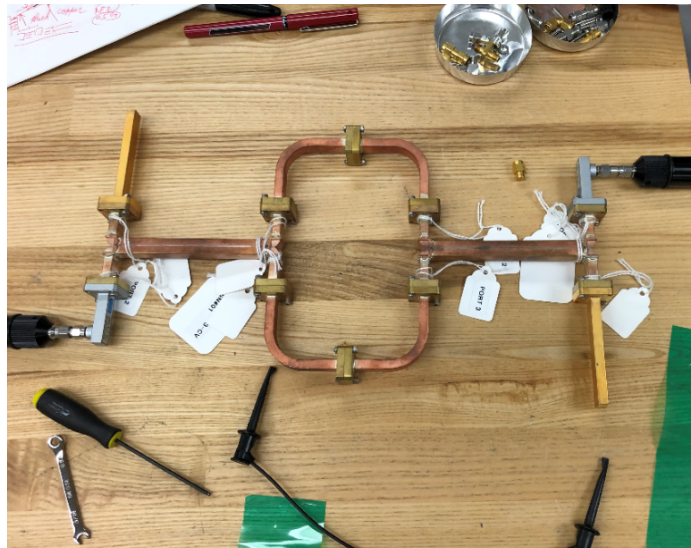


**Figure 14. Two 90-degree hybrids were tested on a network analyzer. These could replace of the magic-T hybrids to provide improved impedance matching.**

## References

- [1] D. Buccino, M. Parisi, D. S. Kahan, M. Paik, Y. M. Yang, W. M. Folkner, and K. Oudrhiri, "Impact of the advanced water vapor radiometer on the Juno gravity science investigation." In *AGU Fall Meeting Abstracts*, vol. 2019, pp. P34A-07, December 2019.
- [2] A. B. Tanner, "Embedding a water vapor radiometer in a DSN antenna: experimental results from DSS 13," *The Technology and Data Acquisition Progress Report*, vol. 42-143, July–September 2000, pp. 1–23, Jet Propulsion Laboratory, Pasadena, California, 15 November 2000.

- [3] A. B. Tanner and J. E. Fernandez, "Embedding a water vapor radiometer in a Deep Space Network ka-band beam-waveguide receiver: a feasibility and performance evaluation," *The Interplanetary Network Progress Report*, vol. 42-149, January–March 2002, Jet Propulsion Laboratory, Pasadena, California, pp. 1–14, 15 May 2002.
- [4] R. Predmore, N. R. Erickson, G. R. Huguenin, P. F. Goldsmith, "A continuous comparison radiometer at 97 GHz," *IEEE MTT-33*, no. 1, January 1985, C.
- [5] C. Bischoff, et al., "The Q/U Imaging Experiment instrument," *The Astrophysical Journal*, 768:9, pp. 28, 01 May 2013. doi:10.1088/0004-637X/768/1/9